Chapter 3

Measurement of Temperature Distribution Based on Optical Fiber-Sensing Technology and Tunable Diode Laser Absorption Spectroscopy

Peng-Shuai Sun, Miao Sun, Yu-Quan Tang, Shuang Yang, Tao Pang, Zhi-Rong Zhang and Feng-Zhong Dong

Additional information is available at the end of the chapter

http://dx.doi.org/10.5772/intechopen.76687

Abstract

Temperature is an important physical quantity in most industrial processes. Distributed temperature sensor (DTS), fiber Bragg grating (FBG), and tunable diode laser absorption spectroscopy (TDLAS) are three primary techniques for temperature measurement using fiber optic sensing and spectrum technology. The DTS system can monitor space temperature field along the fiber in real time. In addition, it also can locate a fire source using two sections of optical fibers which are placed orthogonally to each other. The FBG temperature sensor is used to measure the point temperature. The temperature sensitivity of the bare FBG is 10.68 pm/°C and the linearity is 0.99954 in the range of 30–100°C. Based on tunable diode laser absorption spectroscopy (TDLAS), two-dimensional (2D) distribution reconstructions of gas temperature are realized using an algebraic reconstruction technique (ART). The results are in agreement with the simulation results, and the time resolution is less than 1 s.

Keywords: temperature sensors, optical fiber distributed temperature sensor, fire source localization, fiber Bragg gratings, tunable diode laser absorption spectroscopy

1. Introduction

In recent years, a variety of temperature sensors have been widely applied in petrochemical and other fields to ensure the smooth progress of production and personnel safety [1, 2]. Under normal circumstances, temperature sensors are used to measure the temperature changes for

locating positions of heat points and fire early warning. In addition, the combustion process can be diagnosed and controlled by real-time and accurate monitoring of temperature in the combustion process and emissions of fossil fuels. This chapter briefly introduces temperature field measurement with optical fiber distributed temperature sensor (DTS), fiber Bragg gratings (FBG), and tunable diode laser absorption spectroscopy (TDLAS) based on the research content in our laboratory.

DTS system based on Raman scattering is a kind of real-time and continuous monitoring space temperature field-sensing technology along the fiber direction [3, 4]. The earliest DTS system developed by Dakin et al. achieved a good spatial resolution of 3 m with conventional sensing fiber lengths up to 1 km [5]. Due to the unique advantages of immunity to electromagnetic fields, the easiness of installing wire, and remote-distributed measurement, the DTS system attracts numerous studies, and a long sensing distance of >10 km has been achieved based on Raman backscattering, which can be wildly applied in safety and health monitoring of large infrastructure projects, such as warehousing and oil and gas pipelines [6–9].

Since the first FBG made by Hill [10] at the Canadian Communications Research Center in 1978, FBG has attracted wide attention due to its huge application prospects in optical communication, optical fiber sensing, and integrated optics [11]. FBG utilizes the photosensitive property of the optical fiber material to establish a spatial periodic refractive index distribution on the core of the fiber, which is to change or control the propagation behavior of the light in the region. FBG has been widely used to measure temperature by demodulating the shifts of the Bragg wavelength.

Tunable diode laser absorption spectroscopy (TDLAS) can detect the gas concentration, temperature, flow rate, and pressure with the advantages of fast response, high sensitivity, and undisturbed measurement. It has been widely used for the detection of temperature and temperature distribution [12]. TDLAS is restricted to the flow with near-uniform properties, because it usually measures path-averaged information along the laser beam [13]. Zhou Xin described a two-line absorption temperature sensing based on two H_2O lines with a single laser near 1.8 μm [14]. Nevertheless, quite a few researchers desire to measure the non-uniformity flow fields using one optical beam with multiple absorption lines which is called line-of-sight tunable diode laser absorption spectroscopy (LOS-TDLAS) [15, 16]. The LOS-TDLAS technique only inverts one-dimensional temperature distribution, so it cannot be well applied to the distribution of combustion field. Until recently, a novel method is developed for measuring the two-dimensional (2D) distribution of temperature and gas concentration combined with the computed tomography (CT) which is called tunable diode laser absorption tomography (TDLAT). There are many validation tests about the TDLAT. They have been done on the NASA Langley Direct-Connect Supersonic Combustion Test Facility and the University of Virginia's Supersonic Combustion Facility [17–20]. In addition, a hyperspectral tomography (HT) system has been designed for measuring the 2D distribution of H_2O concentration and temperature simultaneously with a temporal resolution of 50 kHz at 225 spatial grid points [19]. In fact, a combustion control system requires a real-time and fast-response sensor to provide important feedback in the steel-reheating furnace and the thermal power plants. In [21], an online measurement system is described which was designed to monitor the 2D distributions of H_2O mole fraction and temperature on the dynamic flames using TDLAT.

2. The DTS system

2.1. Basic operational principles of the DTS system

An optical fiber-distributed temperature sensor (DTS) system can continuously monitor space temperature field along the fiber length in real time. The temperature information is primarily gained based on spontaneous Raman scattering in optical fiber and optical time domain reflectometry (OTDR) technique. There are various kinds of scattering lights occurred when a short pulse of light is launched into the sensing fiber, such as Rayleigh scattering, Raman scattering, Brillouin scattering, and so on [22]. The frequency of the Rayleigh scattering light is the same as that of the injected light and the intensity is only slightly varying with temperature changes. The Brillouin scattering light is used to simultaneously measure strain and temperature for the sensitivity to changes of strain and temperature. The Raman scattering light is only sensitive to temperature, which is widely used to measure temperature.

There are two scattered components in Raman scattering light [23]. Compared with the frequency of the injected light, the frequency down-shift light is called Stokes (S) Raman scattered light and frequency up-shift light is named anti-Stokes (AS) Raman scattered light. Contrary to the slightly temperature-dependent Stokes Raman scattered light, the intensity of the anti-Stokes Raman scattered light strongly depends on the local fiber temperature. As a result, the intensity of the anti-Stokes Raman scattered light is regarded as the signal light for temperature determination. There are three methods used to demodulate the temperature, which can be described as temperature calculated only using the anti-Stokes Raman scattered light, temperature calculated with the Rayleigh scattered light as the reference light, and temperature calculated with the Stokes scattered light as the reference light.

For the temperature demodulate method, only with the anti-Stokes Raman scattered light, the ratio of the intensity of the anti-Stokes Raman scattered light at temperature T to anti-Stokes Raman scattered light at a known temperature T_0 is used to derive fiber temperature. Photoelectric detector and acquisition card with only one channel are adopted which realizes the cost saving. However, there is a slight fluctuation of the laser energy leading to a measured temperature error. As a result, this method has great instability in the practical application.

The temperature demodulate method using the anti-Stokes Raman scattered light as the signal light and the Rayleigh scattered light as the reference light eliminates the influence of light energy fluctuation. However, the intensity of Rayleigh scattered light is much higher than that of the anti-Stokes Raman scattered light, and the attenuation responses of the two kinds of scattered light are quite different from each other when the fiber is bent [24]. This brings great difficulty to the demodulation of temperature and corrects the temperature error.

While the third temperature demodulate method can solve the above problems. The temperature is calculated by the ratio of the intensity of the anti-Stokes Raman scattered light to Stokes Raman scattered light with the Stokes Raman scattered light seen as the reference light. There is little difference in the magnitude of the anti-Stokes and Stokes Raman scattering light intensity, and the same as the attenuation coefficients. The dual channel demodulation method can make up for the shortage of only using the anti-Stokes Raman scattering light

demodulating temperature, eliminate the influence of light energy fluctuation, and improve the stability of the system. As a consequence, the third method is often used to demodulate the temperature in a DTS system. Thus, the temperature (T) can be derived from the intensity ratio F (T) as follows [25, 26]:

$$F(T) = \frac{\varphi_{AS}(T)}{\varphi_S(T)} = \frac{K_{AS}}{K_S}\frac{\nu_{AS}^4}{\nu_S^4}\exp\left[-(h\Delta\nu/k_BT)\right]\exp\left[-(\alpha_{AS}-\alpha_S)l\right] \quad (1)$$

where φ (T) is the Raman scattering light intensity at temperature T, K is the coefficient concerning Raman scattering cross section, ν is the frequency, h is the Planck constant, Δν is the Raman shift in the transmission medium, and kB is the Boltzmann constant, α is the attenuation coefficient, and l is the location along the fiber.

A reference fiber coil with the length l_0 is maintained at a known temperature T_0. Then, the temperature can be obtained as.

$$\frac{1}{T} = \frac{1}{T_0} - \frac{k}{h\Delta\nu}\ln\left(\frac{F(T)}{F(T_0)}\right) \quad (2)$$

2.2. Brief description of the DTS system

The schematic drawing of the DTS system is presented in **Figure 1**. By using a 1 × 3 wavelength division multiplexer (WDM), the short pulse of light is injected into the sensing fiber and the occurred Raman backscattered lights are injected into a high-performance InGaAs avalanche photodiode (APD). A data acquisition (DAQ) card converts the analog signals transformed by the APD to digital signals. Then, the temperature data are obtained by processing the digital signals with a computer.

In the DTS system, the central wavelength of the pulsed fiber laser is 1550 ± 1 nm with a maximum peak power of 30 W, 10-ns pulse width, and 10-kHz repetition rate. A dual channel high-performance APD is adopted with a circuit bandwidth of 80 MHz. The spectral range of

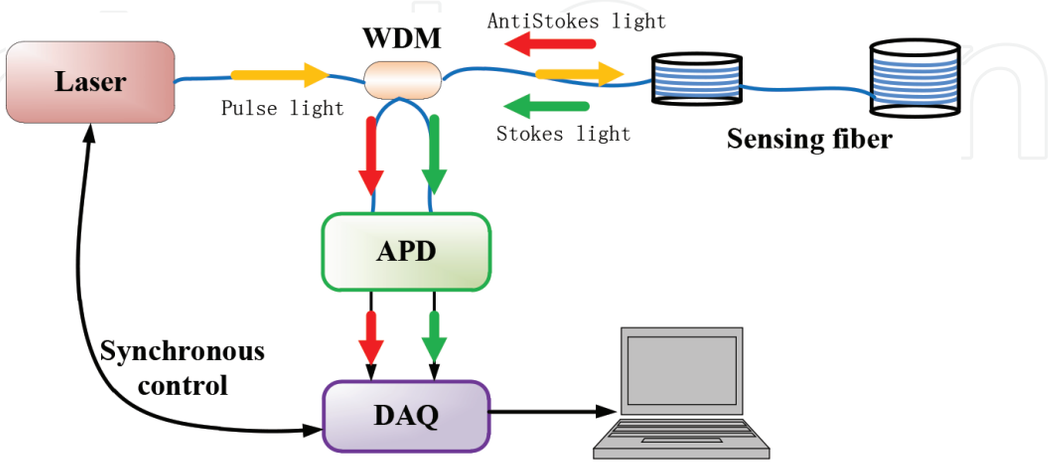

Figure 1. Schematic of the DTS system setup (WDM, wavelength division multiplexer; APD, InGaAs avalanche photodiode; DAQ, data acquisition).

http://dx.doi.org/10.5772/intechopen.76687

the APD is 900—1700 nm, which can fully meet the demand for Raman scattering wavelengths corresponding to the incident wavelength. A dual channel high-speed DAQ card is tailored dedicatedly and specially designed for DTS system applications. The DAQ card uses a network card to transmit data and can perform synchronous sampling up to 100 Ms./s. The real-time linear accumulation average technology is used on the DAQ card with an advantage of zero-time consuming. The highest average number of the DAQ card is 65,535 times, which is suitable for high-speed continuous data acquisition and average measurement applications. **Figure 2** shows the picture of the developed DTS system.

2.3. Experimental results and discussions

Based on the above DTS system, the temperature measurement experiments are conducted to validate the use of the designed DTS system. A length of 124 m optical fiber is used as the reference fiber and is connected with the sensing fiber of 3 km through the FC/APC connector. Two sections of the fiber are selected: (986–1138 m) and (2828—2938 m). The temperature performance of the DTS system is studied by placing the chosen fiber in a temperature-controlled water bath. The temperature of the temperature-controlled water bath is set at 80.0 ± 0.1°C. **Figure 3** shows the measured signal intensities of the anti-Stokes Raman scattered light and Stokes Raman scattered light. The intensities of Raman scattered light both

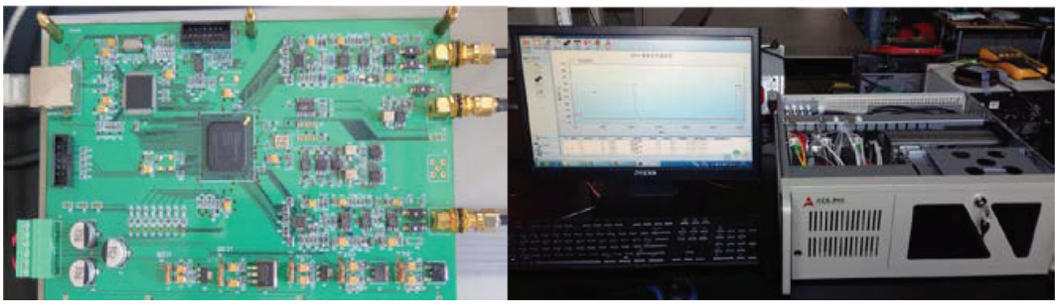

Figure 2. Developed DAQ card and DTS system for temperature measurement.

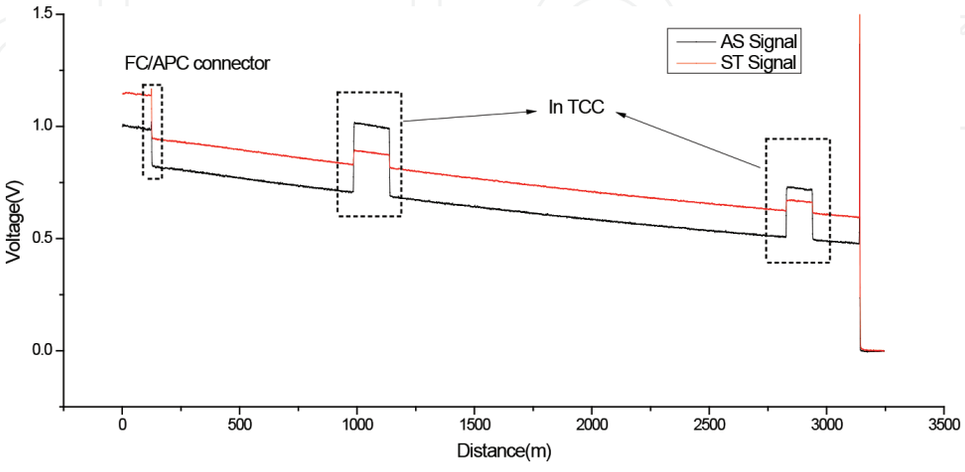

Figure 3. The measured signal intensities of the anti-stokes Raman scattered light and stokes Raman scattered light.

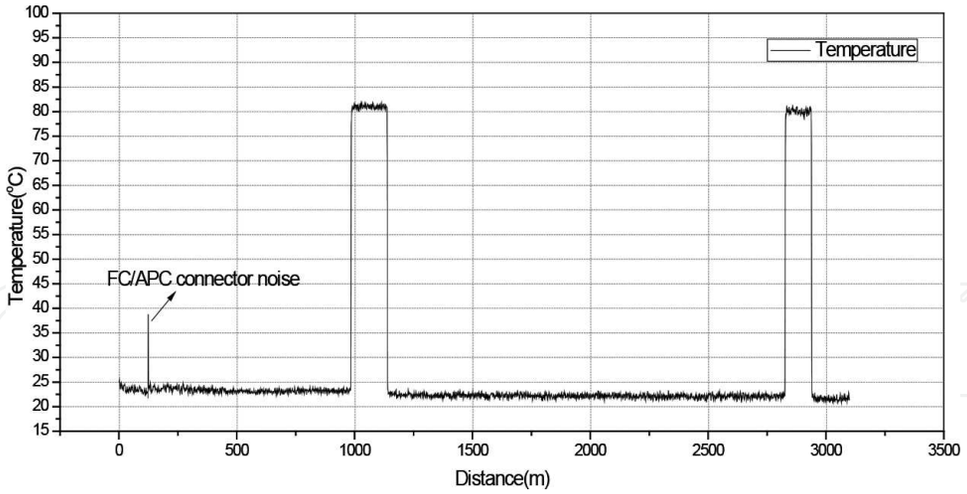

Figure 4. The measured temperature using the DTS system.

change with the temperature rises. However, the intensity change of the anti-Stokes Raman scattered light is much more obvious. The corresponding temperature calculated by the theory presented in Section 2.1 is shown in **Figure 4**.

Due to the advantages of accurate temperature measurement and remote distributed measurement, the DTS system is widely used for the fire warning by measuring the temperature changes and setting up a threshold. Simultaneously, the DTS system is also possible to locate fire sources, which can provide guidance for the timely and effectively extinguishing of fire sources [27, 28].

As shown in **Figure 5**, a fire breakout in a closed room will produce lots of hot gases [29]. The hot gases propagate in shapes similar to that across the ceiling plane of the closed room after the gases rise up to the ceiling. Some assumptions are made to simplify the problem, such as

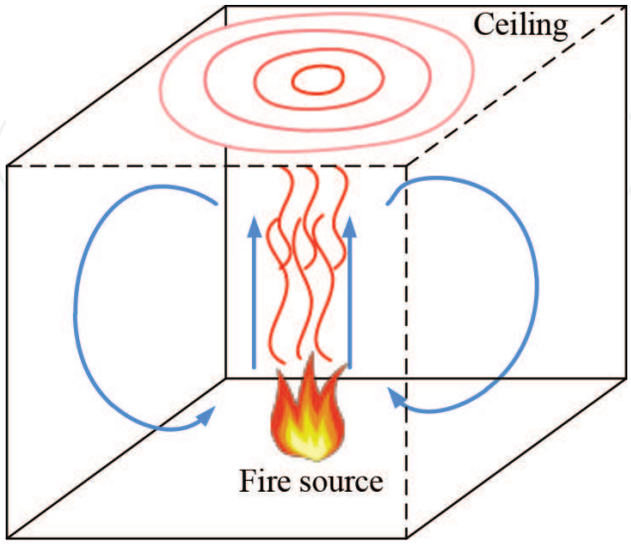

Figure 5. A fire in a closed room.

smooth ceiling of the closed room with a low thermal conductivity, the fire located below the ceiling and not directly at a wall, and so on. Then, the hot gases propagating shapes can be considered as a perfect round. The position of the fire source is situated underneath the center point of the circular shapes in the ceiling plane, which can be calculated by measuring the temperature changes with the DTS system.

Two kinds of methods are proposed to locate a fire source using a DTS system. A section of the dual-line optical fiber or two sections of optical fibers placed orthogonally to each other are used as the sensing elements and installed near the ceiling of a closed room in which the fire source is located. The methods of the source location are verified with experiments using burning alcohol as fire source. Take the fibers on opposite sides of fire source as an example. The coordinates of the alcohol tray center are (45 and 35 cm). When the alcohol is burning, the measured temperature by the DTS system is shown in **Figure 6**. The closer the fiber to the fire source, the higher the measured temperatures. The measured temperature increases fast at the early stage, and the temperature rise rate of the fiber decreases gradually with the burning time increase.

Figure 7 shows the fire source location and errors in dependence of the alcohol burning time. A moving average filter is adopted to reduce the fluctuation of the calculated results. The position of the fire source is depicted in **Figure 8** for a fire burning time of 90 s. The calculated coordinate of the fire source is determined at (45 and 35 cm), which is the same as the actual fire source center.

2.4. Industrial fields and applications

In order to demonstrate the developed DTS system, some preliminary field trials have been carried out at different sites in some circumstances as shown in **Figures 9** and **10**.

Figure 9 shows the test of the mine flameproof DTS system in the coal mine. The measured changes of the temperature indicate that the sensing fibers are placed in coal pillars. As the coal pillars are exposed to the air, the permeated oxygen causes the coal to oxidize and release the

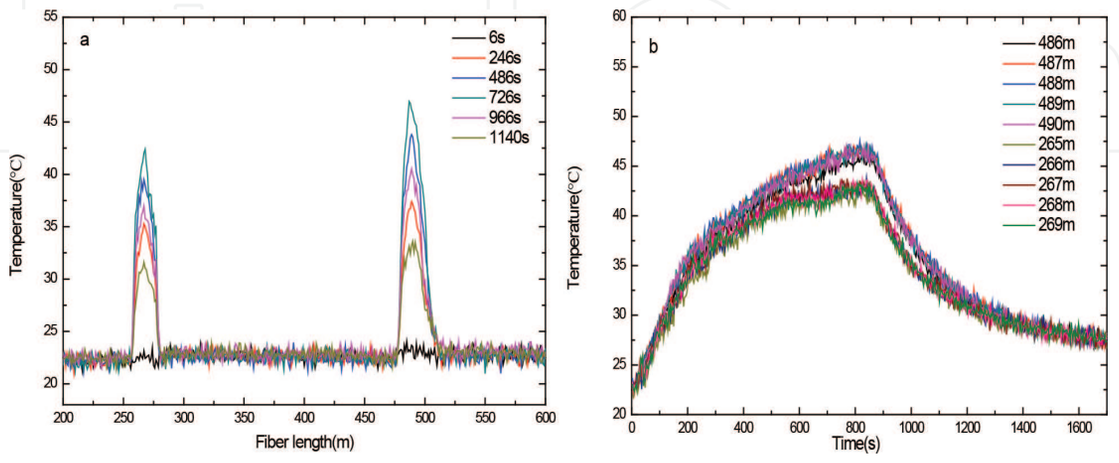

Figure 6. (a) The measured temperature at different burning times. (b) The measured temperature for different fiber lengths.

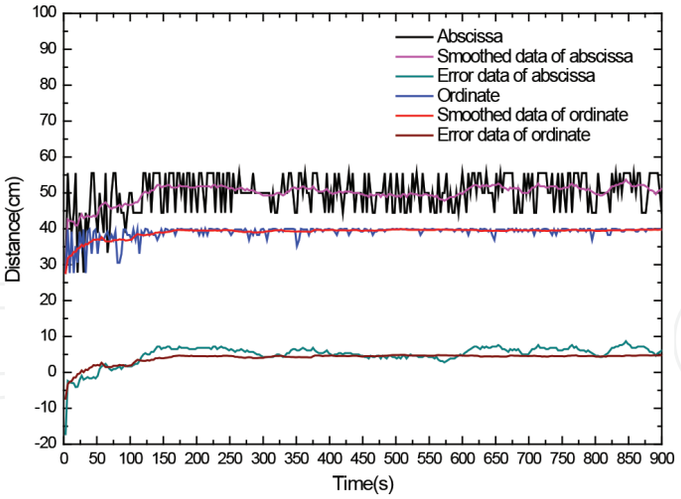

Figure 7. Fire source location and errors in dependence of the alcohol burning time.

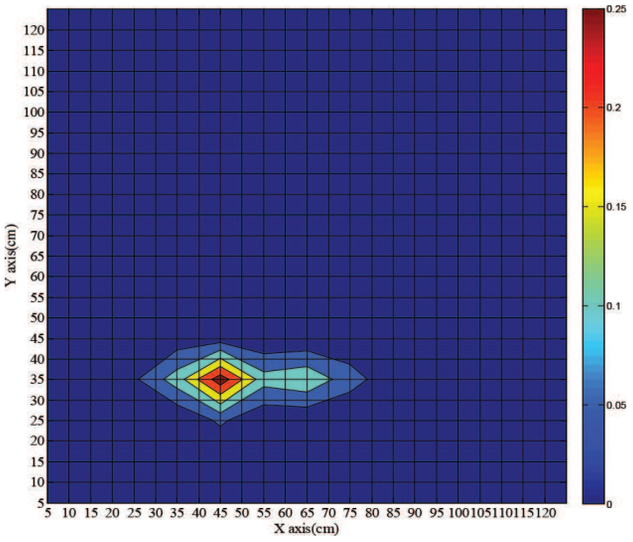

Figure 8. Calculated fire source location with 90-s burning time of the fire.

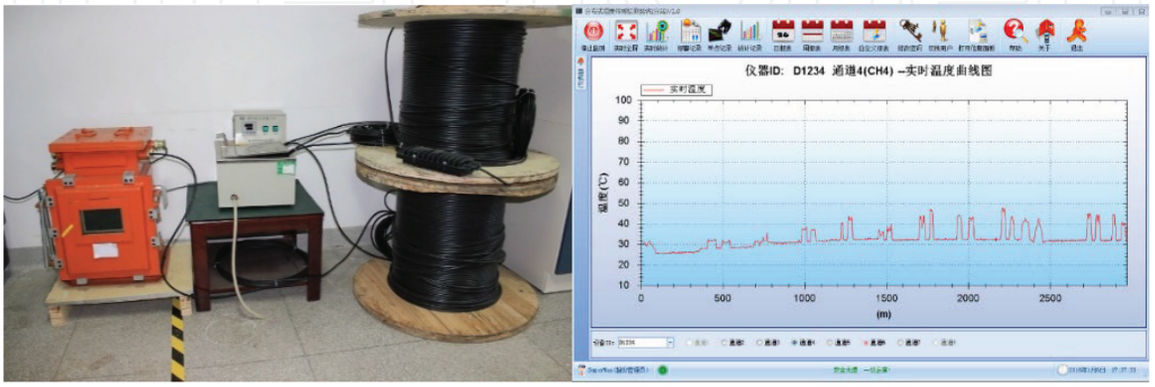

Figure 9. The mine flameproof DTS system and the measured temperature changes in the coal mine.

http://dx.doi.org/10.5772/intechopen.76687

Figure 10. Application of the DTS system to fire monitoring in urban underground comprehensive pipe corridor.

heat, causing the internal temperature to be higher than the external temperature. **Figure 10** shows a fire safety distributed optical fiber fire detector, which can be used for fire detection and alarm in most situations.

3. The FBG temperature sensor

3.1. Measurement principle of the FBG temperature sensor

When the external temperature or strain changes, the period of FBG and the refractive index of the core will change, which cause the change of the Bragg wavelength of the FBG. In addition, the Bragg wavelength of the FBG follows the change of these quantities, which is the basic principle of the FBG as the wavelength modulation sensor. As long as the wavelength change of FBG can be measured, the strain and temperature of FBG can be obtained. Therefore, it is the most important to master the rule of FBG wavelength varying with these quantities.

As shown in **Figure 11**, a broadband light source is injected into the optical fiber, and the grating reflects the narrowband spectral components of the Bragg wavelength. The component of the spectrum is lost in the transmission light. The bandwidth of the reflected signal depends on several parameters, especially the length of the FBG, but is usually 0.05–0.3 nm [30] in most

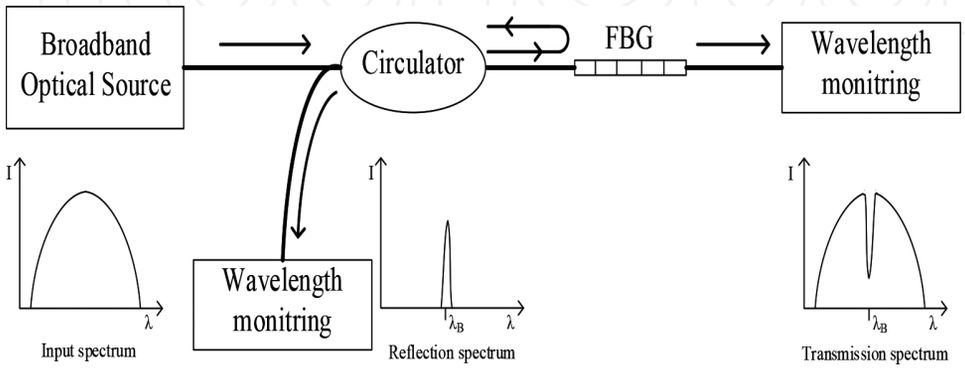

Figure 11. The schematic of the FBG-based sensor system with reflective or transmissive detection options.

FBG sensor applications. The perturbation of the FBG leads to the offset of the Bragg wavelength of the sensor, which can be detected in the reflection or transmission spectrum. From the coupled-mode theory [31], the expression of the FBG equation is expressed as follows:

$$\lambda_B = 2n_{eff}\Lambda \tag{3}$$

It is known that the Bragg wavelength λ_B varies with the change of the equivalent refractive index n_{eff} and the period Λ of the FBG. The equivalent refractive index and the period of FBG vary with the change of strain and temperature, which can be written in the following form:

$$\lambda_B = 2n_{eff}(\varepsilon, \mathrm{T})\Lambda(\varepsilon, \mathrm{T}) \tag{4}$$

By differential

$$\begin{aligned} d\lambda_B = &\left[2\Lambda\left(\frac{\partial n_{eff}}{\partial \varepsilon}\right)_{T=c1} + 2n_{eff}\left(\frac{\partial \Lambda}{\partial \varepsilon}\right)_{T=c1}\right]d\varepsilon \\ &+\left[2\Lambda\left(\frac{\partial n_{eff}}{\partial T}\right)_{\varepsilon=c2} + 2n_{eff}\left(\frac{\partial \Lambda}{\partial T}\right)_{\varepsilon=c2}\right]dT \end{aligned} \tag{5}$$

Deformed to

$$\begin{aligned} d\lambda_B = &\left[2n_{eff}\Lambda\left(\frac{1}{n_{eff}}\frac{\partial n_{eff}}{\partial \varepsilon}\right)_{T=c1} + 2n_{eff}\Lambda\left(\frac{1}{\Lambda}\frac{\partial \Lambda}{\partial \varepsilon}\right)_{T=c1}\right]d\varepsilon \\ &+\left[2n_{eff}\Lambda\left(\frac{1}{n_{eff}}\frac{\partial n_{eff}}{\partial T}\right)_{\varepsilon=c2} + 2n_{eff}\Lambda\left(\frac{1}{\Lambda}\frac{\partial \Lambda}{\partial T}\right)_{\varepsilon=c2}\right]dT \end{aligned} \tag{6}$$

Simplify to

$$\frac{d\lambda_B}{\lambda_B} = \left[\left(\frac{1}{n_{eff}}\frac{\partial n_{eff}}{\partial \varepsilon}\right)_{T=c1} + \left(\frac{1}{\Lambda}\frac{\partial \Lambda}{\partial \varepsilon}\right)_{T=c1}\right]d\varepsilon + \left[\left(\frac{1}{n_{eff}}\frac{\partial n_{eff}}{\partial T}\right)_{\varepsilon=c2} + \left(\frac{1}{\Lambda}\frac{\partial \Lambda}{\partial T}\right)_{\varepsilon=c2}\right]dT \tag{7}$$

Further rewrite to

$$\frac{\Delta\lambda_B}{\lambda_B} = \left[\frac{1}{n_{eff}}\frac{\partial n_{eff}}{\partial \varepsilon} + \frac{1}{\Lambda}\frac{\partial \Lambda}{\partial \varepsilon}\right]\Delta\varepsilon + \left[\frac{1}{n_{eff}}\frac{\partial n_{eff}}{\partial T} + \frac{1}{\Lambda}\frac{\partial \Lambda}{\partial T}\right]\Delta T \tag{8}$$

According to the definition of thermal expansion coefficient, thermal coefficient and strain, and the theory of elastic effect

$$\begin{aligned} &\frac{1}{\Lambda}\frac{\partial \Lambda}{\partial T} = \alpha_F \\ &\frac{1}{n_{eff}}\frac{\partial n_{eff}}{\partial T} = \xi \\ &\frac{1}{\Lambda}\frac{\partial \Lambda}{\partial \varepsilon} = 1 \\ &\frac{1}{n_{eff}}\frac{\partial n_{eff}}{\partial \varepsilon} = -p_\varepsilon \end{aligned} \tag{9}$$

where α_F is the thermal expansion coefficient of the fiber, the ξ is the thermal optical coefficient of the fiber, and the P_ε is the effective elastic coefficient of the fiber. For a finished fiber, the above coefficients are constant, so.

$$\frac{\Delta\lambda_B}{\lambda_B} = (1 - p_\varepsilon)\Delta\varepsilon + (\alpha_F + \xi)\Delta T \tag{10}$$

where $\Delta\varepsilon$ and ΔT are the changes of strain and temperature, respectively. When the FBG is not affected by the strain, the upper formula can be rewritten as.

$$\Delta\lambda_B = \lambda_B(\alpha_F + \xi)\Delta T \tag{11}$$

It can be seen that the temperature-sensing characteristics of the FBG are caused by the thermal light effect and thermal expansion effect of the FBG. The effective refractive index of FBG is changed by thermo-optic effect, while the thermal expansion effect causes the grating periodic change, resulting in the variation of wavelength of the FBG reflection peak. The wavelength of the FBG varies with the temperature, as shown in Eq. (11). To measure the wavelength change of the FBG, the temperature of the FBG can be obtained, which is the basic principle of the FBG sensors.

From Eq. (11), the sensitivity coefficient of FBG depends on the material itself. Therefore, using FBG as temperature sensor can get a good linear output. Generally, the linear thermal expansion coefficient of fused silica fiber is α_F = 5.0 × 10^{-7}/°C~5.5 × 10^{-7}/°C, the thermal optical coefficient of the fiber is ξ = 6.0 × 10^{-6}/°C~1.0 × 10^{-5}/°CC [32–38]. The temperature sensitivity of FBG at different center wavelengths is given in α_F = 5.5 × 10^{-7}, ξ = 6.4 × 10^{-6}/°C as an example, as shown in **Table 1**.

It can be seen that the temperature sensitivity of fused silica FBG is essentially determined by the refractive index and temperature coefficient of the material, without considering the external factors. At present, the temperature sensitivity of the bare FBG is about 10 pm/°C [30, 32, 33], and the FBG demodulator with the resolution of 1 pm [39] can provide temperature measurement of 0.1°C. The temperature response of the Bragg wavelength of FBG is measured in the range of 30–100°C. In the experiment, a λ_B is recorded for each change of temperature at 10°C for Bragg wavelength detection. The test result is shown in **Figure 12**. The experimental results show that the temperature sensitivity of the bare FBG is 10.68 pm/°C and the linearity is 0.99954, which shows that the linearity is very good.

Wavelength (nm)	Temperature sensitivity (pm/°C)	Wavelength (nm)	Temperature sensitivity (pm/°C)
1310	9.10	1545	10.74
1340	9.31	1550	10.77
1350	9.38	1555	10.81
1540	10.70	1560	10.84

Table 1. Temperature sensitivity of FBG at different Bragg wavelengths.

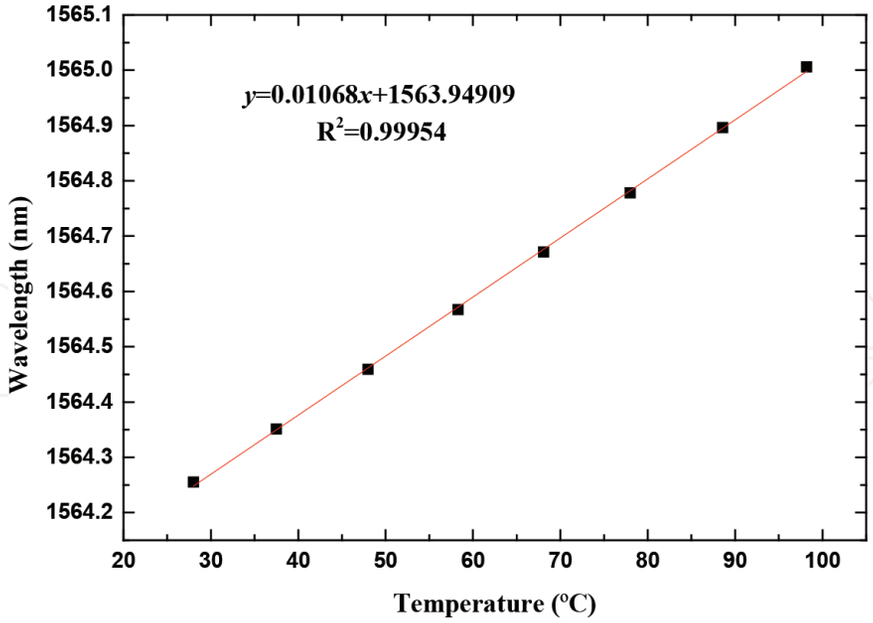

Figure 12. Relation of the temperature and the Bragg wavelength.

3.2. Research progress and practical application of the FBG temperature sensor

Since 1978, people first successfully write gratings in germanium-doped fibers, the fabrication of FBG has been formally started. From 1978 till now, the fabrication technology of FBG has made great progress, and many writing methods and practical techniques have been studied. The fabrication methods of FBG can be divided into internal writing method [10], interference method [40], point-by-point writing method [41], and phase mask writing method [42]. The phase mask writing method is widely applied because of its advantages such as simple process, good reproducibility, high yield, and large-scale production.

Temperature is a factor that directly affects the wavelength change of FBG. It is used directly as a direct application of bare FBG as a temperature sensor [43, 44]. Usually, FBG cannot be used directly as a sensor because of the stiffness and vulnerability of the fiber. Like many other types of sensors, FBG temperature sensors also need to be encapsulated. The main role of encapsulation technology is protection and sensitization, and it is hoped that FBG can have a strong mechanical strength and a longer life span. At the same time, it is also hoped that the sensitivity of FBG response to temperature can be improved by appropriate encapsulation technology in optical fiber sensing. The commonly used packaging methods are base sheet type, metal tube type, polymer encapsulation mode [32, 33, 45], and so on. As shown in **Figure 13**, it is a metal tube type encapsulated temperature sensor used in our laboratory.

On the other hand, some new technologies are also introduced to FBG temperature-sensing technology to improve the performance of FBG temperature sensors such as the use of doping in the optical fiber special impurities [46], femtosecond laser grating [47], D fiber [48], polymer-coated [49], and other methods to improve the temperature measurement range of FBG. These sensors can measure temperature at high temperature or ultra-low temperature conditions. At present, FBG temperature sensor has been widely used in many fields, such as medical [50],

http://dx.doi.org/10.5772/intechopen.76687

Figure 13. Metal tube type encapsulated FBG temperature sensor.

Figure 14. Installation diagram of FBG temperature sensor.

structural health monitoring [51], nuclear industry [52], electric power systems [53], and so on. But in most applications, the cross-sensitivity problem of temperature and strain of FBG sensors is urgently needed to solve, and this research was also conducted extensively [54–57].

The FBG sensor is mainly used in the safety monitoring system of coal mine. As shown in **Figure 14**, the FBG temperature sensor is fixed near the measuring point by binding and welding. Six FBG temperature sensors are mounted on the second layer of the vent of the mine shaft, and the real-time monitoring results of the sensor are shown in **Figure 15**. The FBG

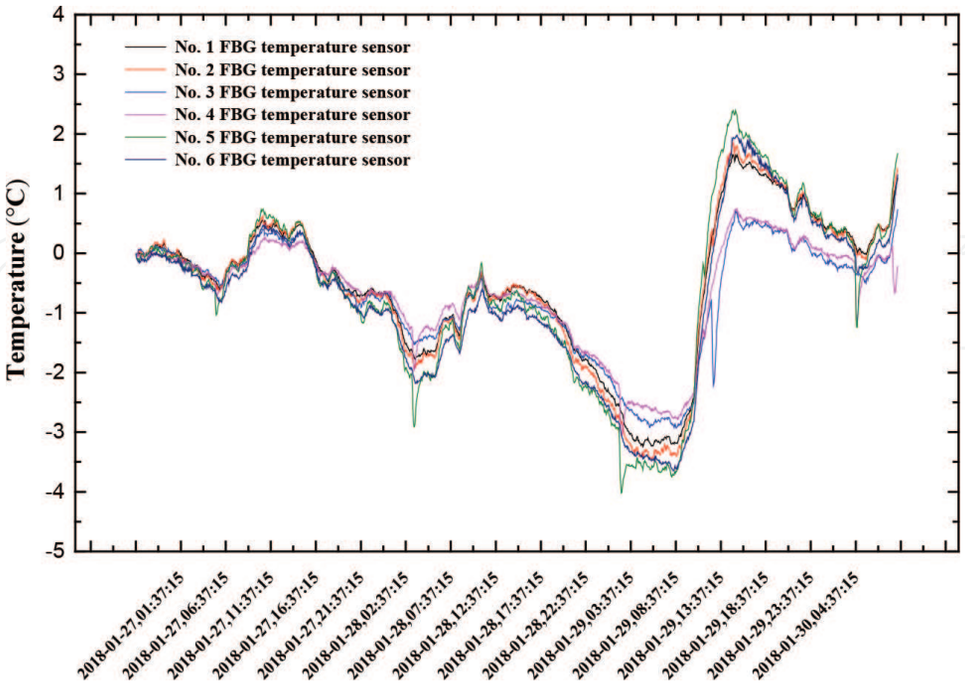

Figure 15. The real-time monitoring results of FBG sensors on the second layer of the vent of the mine shaft.

temperature sensor can be used to monitor the air temperature in the mine in real time, which can be used to provide data and early warning for the monitoring demand of the hidden danger of the coal mine fire.

4. The TDLAS temperature measurement system

4.1. The principles of TDLAS

The TDLAT includes TDLAS and CT technology. The TDLAS is used to measure the spectral information of the laser beam path, and the CT technology is used for calculating the 2D images of gas concentration and temperature. According to the Lambert–Beer law, the laser beams at frequency v [cm^{-1}] through the measure region with a path length of L [cm], the absorbance α_v can be expressed as [58].

$$\alpha_v = \int_0^L PCST\varphi dl \tag{12}$$

where C is the target gas concentration, P [atm] is the local total pressure, φ [cm] is the normalized line shape function, and T [K] is the local temperature. For atmosphere pressure and a high temperature, the line shape is usually approximated by a Voigt profile [59, 60]. The line strength of molecular transition S [T] [cm^{-2} atm^{-1}] is a function of temperature as follows [61]:

$$S(T) = S(T_0)\frac{Q(T_0)}{Q(T)}\frac{T_0}{T}\,exp\left[-\frac{hcE_i''}{k}\left(\frac{1}{T}-\frac{1}{T_0}\right)\right]\left[1-\,exp\left(\frac{-hcv_{0,i}}{kT}\right)\right]\left[1-\,exp\left(\frac{-hcv_{0,i}}{kT_0}\right)\right]^{-1} \tag{13}$$

where T_0 [K] is the reference temperature, h [J·s] is Planck's constant, k [J/K] is Boltzmann's constant, c [cm/s] is the light speed, v_0 [cm^{-1}] is the line-center frequency, E'' [cm^{-1}] is the lower state energy of the transition, v_0 and $Q(T)$ is the partition function of the absorbing molecule [62]. Because the line-shape function φ is normalized $\int\varphi dv \equiv 1$, the integrated absorbance A_v [cm^{-1}] can be inferred from Eq. (12).

$$A_v = \int_{-\infty}^{+\infty}\alpha_v dv = \int_0^L PCSTdl \tag{14}$$

The integrated absorbance of two transition lines is measured simultaneously with the same concentration, pressure, and path length. Beside the double-line thermometry [63], the ratio of two absorbances can be further simplified to Eq. (14). R is the ration which is a function of temperature only as expressed.

$$R(T) = \frac{A_1}{A_2} = \frac{S_1(T)}{S_2(T)} = \frac{S_1(T_0)}{S_2(T_0)}\,exp\left[-\frac{hc}{k}\left(E_1'' - E_2''\right)\left(\frac{1}{T}-\frac{1}{T_0}\right)\right]. \tag{15}$$

Then, the temperature can be calculated by the following equation:

http://dx.doi.org/10.5772/intechopen.76687

$$T = \frac{\frac{hc}{k}\left(E_2'' - E_1''\right)}{\ln R + ln\frac{S_2(T_0)}{S_1(T_0)} + \frac{hc}{k}\frac{E_2'' - E_1''}{T_0}} \tag{16}$$

Each line integrated absorbance A_v can be obtained by fitting Voigt line shape. The gas concentration can be calculated from the integrated absorbance within the known temperature, pressure and path length using Eq. (14). However, the calculated concentration and temperature are the path-averaged value along the line of sight. For the 2D distributions of gas concentration and temperature in the ROI (region of interest), it is divided into $M \times N$ grids, as shown in **Figure 16**. In each grid, the target gas concentration and temperature are assumed to be uniform. The optical path length $L_{i,j}$ of the i-th laser beam within the j-th grid can be calculated according to the two intersecting positions of the grid and beam. It is obvious that the tomographic image pixels and accuracy rely on the number of views, laser beams, and discretized grids.

According to Eq. (14), the integrated absorbance of the i-th laser beam $A_{v,i}$ can be expressed as Eq. (17).

$$A_{v,i} = \sum_{j}^{M\times N} \alpha_{v,j} L_{i,j} = \sum_{j}^{M\times N} [PS(v,T)C]_{v,j} \tag{17}$$
$$(i = 1,2\ldots I; j = 1,2\ldots M \times N)$$

where $\alpha_{v,i}$ is the absorption coefficient in the j-th grid. I and $M \times N$ are the number of beams and total grid, respectively. Actually, Eq. (17) is more easily understood to be rewritten in matrix equation as Eq. (18).

$$\begin{bmatrix} L_{1,1} & L_{1,2} & \cdots & L_{1,M\times N} \\ L_{2,1} & L_{2,2} & \cdots & L_{2,M\times N} \\ \vdots & \vdots & \vdots & \vdots \\ L_{I,1} & L_{I,2} & \cdots & L_{I,M\times N} \end{bmatrix} \begin{bmatrix} \alpha_1 \\ \alpha_2 \\ \vdots \\ \alpha_{M\times N} \end{bmatrix}_v = \begin{bmatrix} A_1 \\ A_2 \\ \vdots \\ A_I \end{bmatrix}_v . \tag{18}$$

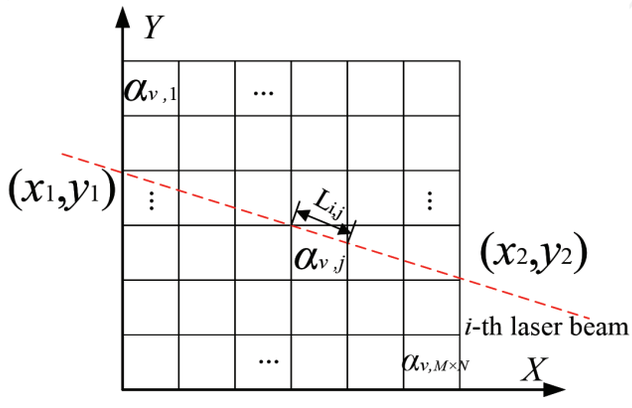

Figure 16. A geometric description of a projection beam and ROI.

The matrix $\boldsymbol{L}$ can be determined by a geometrical arrangement. The integrated absorbances of two lines $\boldsymbol{A_{v1}}$ and $\boldsymbol{A_{v2}}$ are obtained by measurements. In this work, we can calculate the absorption coefficients $\boldsymbol{\alpha_v}$ using the algebraic reconstruction technique (ART) to solve the linear equation [64]. Equation (19) is the iterative formula to solve the linear equation.

$$\alpha_j(k+1) = \alpha_j(k) + \lambda \frac{A_i - \sum_{j=1}^{M\times N} \alpha_j(k) L_{i,j}}{\sum_{j=1}^{M\times N} {L_{i,j}}^2} L_{i,j} \quad (i = 1, 2....I; j = 1, 2...M \times N) \tag{19}$$

where λ ($0 < \lambda < 2$) is the relaxation coefficient which plays an important role in determining convergence rate and accuracy performance, k is the iteration index in the iterative process [65]. To modify a more effective imaging algorithm, the λ of conventional ART should be replaced by an automatic adjustment relaxation parameter in time of the iterative process [66]. The λ of Eq. (19) can be expressed as.

$$\lambda = \beta \frac{\alpha_j(k) L_{i,j}}{\sum_{j=1}^{M\times N} \alpha_j(k) L_{i,j}} \tag{20}$$

where β is a constant where the value would be recommended for from 0.1 to 0.3. It depends on the number of grids and beams. As shown in Eq. (21), the ε is the difference between two absorption coefficients in the iterative process. The iteration will be terminated when the ε is less than 1×10^{-6}.

$$\alpha_j(k+1) - \alpha_j(k) \le \varepsilon \left(\varepsilon = 10^{-6}\right) \tag{21}$$

The absorbances $\alpha_{v1,j}$ and $\alpha_{v2,j}$ in the j-th grid are obtained by performing the ART. Finally, the temperature T_j in j-th grid can be retrieved from Eqs. (15) and (16), the H_2O concentration can be calculated from Eq. (22).

$$C_j = \frac{\alpha_{v1,j}}{S_1\left(T_j\right)} \tag{22}$$

4.2. The typical system

Figure 17(a) shows a typical system of TDLAT. **Figure 17(b)** shows a photograph of the optical test section and the configuration of the probe beams: eight vertically and eight horizontally, and the neighboring probe beams have a 4-cm spacing. To be specific, the diode laser controller provides a stable temperature and a precise current controlling for a DFB laser. Two H_2O absorption lines included $v_1 = 7164.91\ cm^{-1}$ and $v_2 = 7165.84\ cm^{-1}$ can be covered by the signal generator which can produce a saw-tooth scanning current. Then, the output laser is split into 16 channels by a 1×16 splitter. Each channel output beam is firstly collimated by a collimator and then guided through the region of interest. Finally, the laser beam comprising absorption information is sampled by the photodetector. The signal of 16 channels is transferred into the Personal Computer simultaneously for reconstructing the 2D distributions of H_2O concentration and temperature. In this process, a LabVIEW program is used to perform the data sampling and processing.

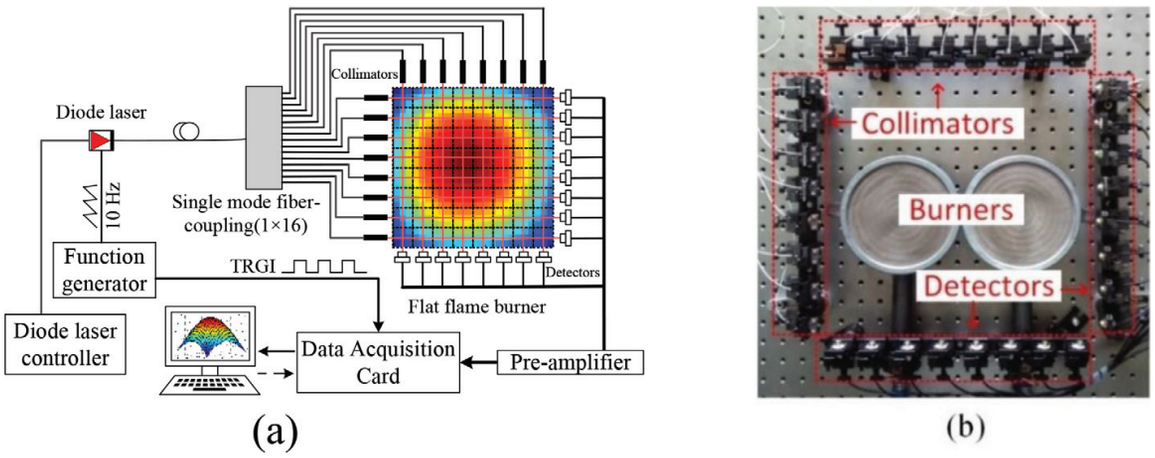

Figure 17. The experimental system. (a) The scheme of the TDLAT system with 8 × 8 grids, (b) the photograph of the optical section: Right and under are 16 detectors, left and upper are 16 collimators.

4.3. Experimental setup and results

Based on the above TDLAT system, a series of experiments have been done. The output wave number of DFB laser requires to be measured before the test started. The result shows that the variation is 0.032 cm^{-1}/mA and it is inversely proportional to the laser drive current. **Figure 18** shows the relationship between the laser wave number and the drive current under different temperatures. In the experiments, the drive current is set from 63 to 118 mA and the laser temperature is stabilized at 31°C. The wave number range of laser transmission is from 7164.64 to 7166.40 cm^{-1} which cover the two H_2O absorption lines. Meanwhile, all the absorption spectrums are fit by the Voigt line-shape function. **Figure 19** shows the direct absorption signals in room air (black dot line) and in flame (red solid line) for two H_2O absorption lines at v_1 = 7165.82 and v_2 = 7164.91 cm^{-1}, respectively. At last, the distributions of H_2O concentration and temperature can be calculated by the modified ART. In the case of computing efficiency, one image of 2D distributions can be updated and displayed for less than 1 s. In the future work, we could increase the scanning frequency to hundred or thousand times to meet the different combustion states.

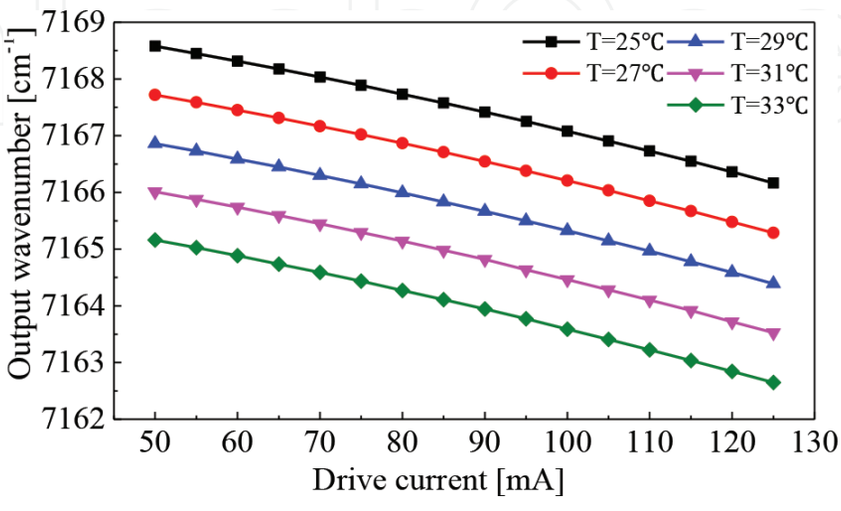

Figure 18. The relationship of the laser wave number and drive current at different operation temperatures.

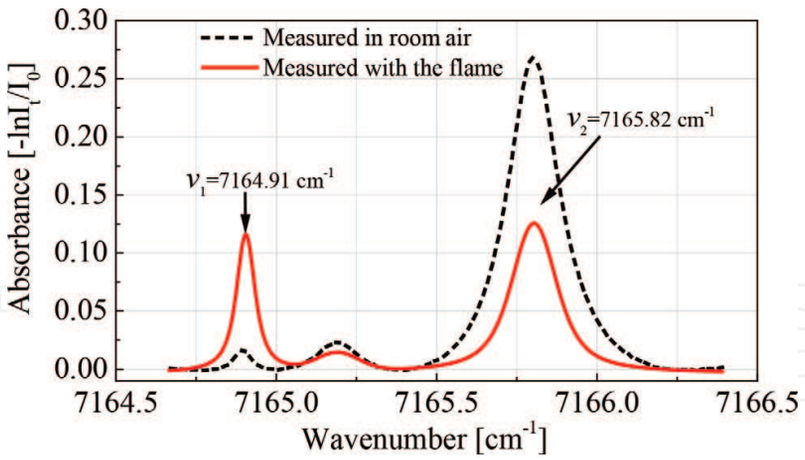

Figure 19. The direct absorption signals in the flame (red solid line) and in room air (black dot line) for two transitions at v_1 = 7164.91 and v_2 = 7165.82 cm^{-1}, respectively.

In this experiment, a premixed flame is generated by a circular flat flame burner which is shown in **Figure 20**. The air and gas fuel were mixed in a buffering zone and then through the honeycomb grids before flying into the flame region. At the same time, the gas flow rate is accurately controlled using two float-type flow meters. As shown in **Figure 21**, the side length of the square measurement region is 32 cm and the diameter of the burner is 12 cm. The height of the laser beams is adjusted to 2 cm above the burner surface. Therefore, the image of 2D distributions of the H_2O concentration and temperature is the cross section of the flame at H = 2 cm. In the series of experiments, the air flow rate is set to 20 L/min, and three different combustion states are operated by setting the gas fuel (CH_4) flow rates to 2.1, 1.6, and 1.0 L/min, which results in the fuel-air equivalence ratio (ϕ) approximate to 1, 0.75, and 0.5, respectively. The 2D distributions of H_2O concentration C^{cal} and temperature T^{cal} are able to reconstruct, when the flame is stabilized.

As shown in **Figure 22(a)**, the cubic spline interpolating function is applied to smooth the reconstructed image [67]. The value of C^{cal} and T^{cal} in the flame core is larger than the flame edge. The three peaks of temperature are 955, 992, and 1127 K under three different kinds of equivalence ratios, respectively. Most obviously, when the equivalence ratio of the premixed flow is exactly stoichiometric, the combustion temperature will reach the highest. For comparison purposes, a B-type thermocouple has been used to measure the temperature of the core flame, and the results are 905, 970, and 1066 K under three different equivalence ratios,

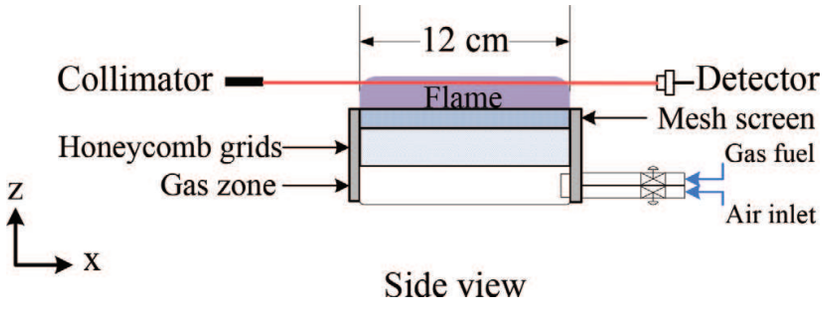

Figure 20. Schematic of the burner.

http://dx.doi.org/10.5772/intechopen.76687

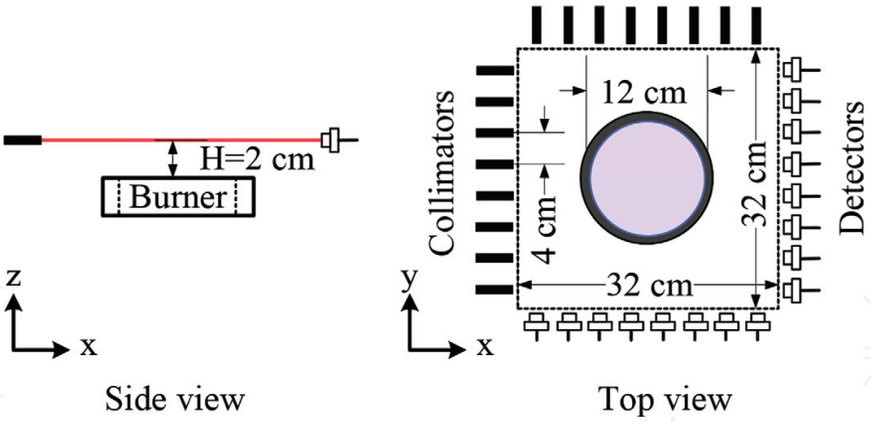

Figure 21. The geometric description of one burner to generate a symmetrical flame shape.

respectively. We can calculate the temperature relative errors, which are less than 5.6%, between the peak value of T^{cal} and the B-type thermocouple. As shown in **Figure 22(b)**, the case of the H_2O concentration C^{cal} distribution is quite like the distribution of T^{cal}. We can calculate the theoretical value of H_2O concentration using chemical equilibrium method under the different fuel-air equivalence ratio. The results show that the H_2O concentrations are 0.190, 0.146, and 0.099 while the fuel-air equivalence ratios are 1, 0.75, and 0.5, respectively. In contrast, the measurement values are 0.174, 0.135, and 0.092 in the core flame under three combustion states. Therefore, the relative errors of C^{cal} between theoretical value and the measurement are less than 8.6%. The errors are mainly produced by the flow disturbance and the flame region which can cause the H_2O concentration to be lower than its theoretical value.

A TDLAT sensor was developed for the simultaneous tomographic imaging of temperature and species concentration. The distribution images of temperature and H_2O mole fraction are

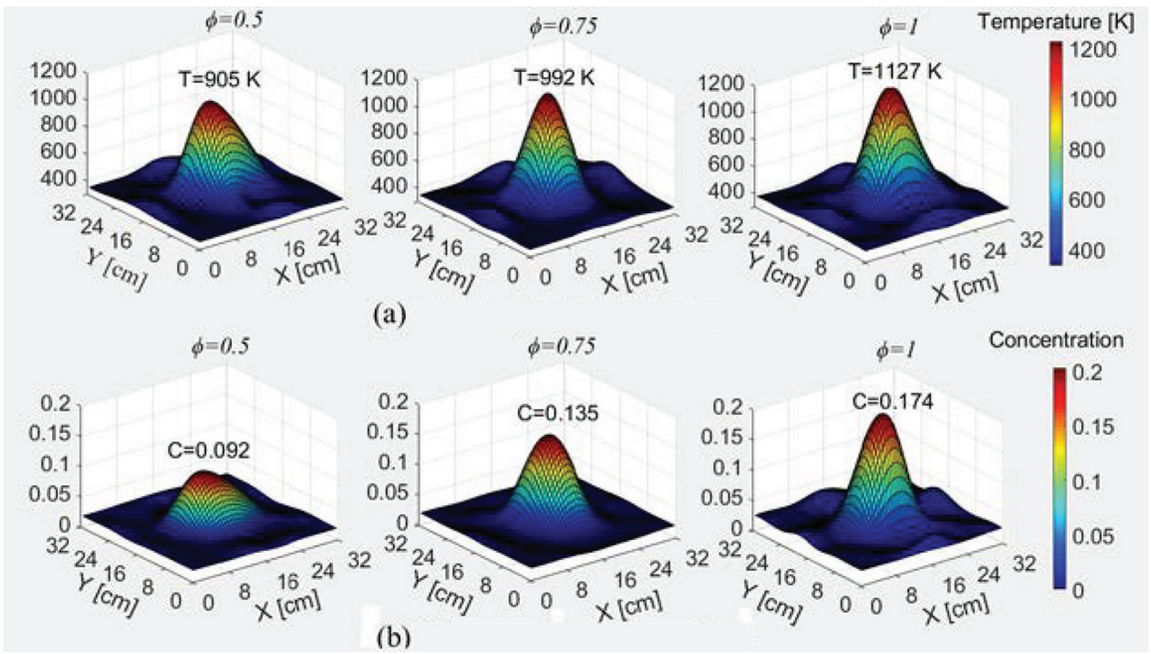

Figure 22. The results of distributions under three kinds of fuel-air equivalence ratio (ϕ). (a) Temperature distributions and (b) H_2O concentration distributions.

carried out during three combustion states, and the time resolution is less than 1 s. The spatial and temporal resolutions can be increased by improving the scan frequency of DFB laser and data-processing algorithms in the future.

5. Conclusions

In this chapter, three temperature measuring methods with DTS, FBG, and TDLAS are introduced in detail. The DTS system can continuously monitor space temperature field along the fiber length in real time. It is widely used for a fire safety distributed optical fiber fire detector and alarm, such as the field of coal mine security. Simultaneously, the DTS system is also to locate fire sources in the three-dimensional space. The FBG temperature sensor can measure the temperature using the Bragg wavelength change. It had been widely applied in the safety monitoring system of coal mine. The temperature sensitivity of the bare FBG is 10.68 pm/°C and the linearity is 0.99954. The TDLAT sensor is a new effective method for the reconstruction of the temperature and H_2O concentration distribution. The distribution images of temperature and H_2O mole fraction are carried out during three combustion states, and the time resolution is less than 1 s. Furthermore, it exhibits a good potential for combustion flame monitoring. The dynamic flame shape diagnosis can be used for combustion feedback control in order to maintain combustion efficiency and minimize pollutant emissions during their operation life cycle.

Acknowledgements

This work is partly supported by the National Natural Science Foundation of China (Grant Nos. 41775128, 41405034, and 11204319), the External Cooperation Program of the Chinese Academy of Sciences (Grant No. GJHZ1726), the Special Fund for Basic Research on Scientific Instruments of the Chinese Academy of Science (Grant No. YZ201315), and the Chinese Academy of Science President's International Fellowship Initiative (PIFI, 2015VMA007).

Author details

Peng-Shuai Sun[1], Miao Sun[2], Yu-Quan Tang[1,3], Shuang Yang[1,4], Tao Pang[1,3], Zhi-Rong Zhang[1] and Feng-Zhong Dong[1,3,4]*

*Address all correspondence to: fzdong@aiofm.ac.cn

1 Anhui Provincial Key Laboratory of Photonic Devices and Materials, Anhui Institute of Optics and Fine Mechanics, Chinese Academy of Sciences, Hefei, Anhui, China

2 School of Electronic and Information Engineering, Hefei Normal University, Hefei, China

3 Key Laboratory of Environmental Optics and Technology, Anhui Institute of Optics and Fine Mechanics, Chinese Academy of Sciences, Hefei, China

4 University of Science and Technology of China, Hefei, China

References

[1] Li H-N, Li D-S, Song G-B. Recent applications of fiber optic sensors to health monitoring in civil engineering. Engineering Structures. 2004;**26**:1647-1657. DOI: 10.1016/j.engstruct.2004.05.018

[2] Chan THTYL, Tam HY, et al. Fiber Bragg grating sensors for structural health monitoring of Tsing Ma bridge: Background and experimental observation. Engineering Structures. 2006;**28**:648-659. DOI: 10.1016/j.engstruct.2005.09.018

[3] Wang ZL, Zhang SS, Chang J. Adaptive data acquisition algorithm in Raman distributed temperature measurement system. Optik. 2014;**125**:1821-1824. DOI: 10.1016/j.ijleo.2013.08.048

[4] Hausner MB, Suarez F, Glander KE. Calibrating single-ended fiber-optic Raman spectra distributed temperature sensing data. Sensors (Basel). 2011;**11**:10859-10879. DOI: 10.3390/s111110859

[5] Dakin J, Pratt D, Bibby G. Temperature distribution measurement using Raman ratio thermometry. Fiber Optic and Laser Sensors III: International Society for Optics and Photonics; 1986. p. 249-257

[6] Bolognini G, Hartog A. Raman-based fibre sensors: Trends and applications. Optical Fiber Technology. 2013;**19**:678-688. DOI: 10.1016/j.yofte.2013.08.003

[7] Vercauteren N, Huwald H, Bou-Zeid E. Evolution of superficial lake water temperature profile under diurnal radiative forcing. Water Resources Research. 2011;**47**:W09522. DOI: 10.1029/2011WR010529

[8] Yilmaz G, Karlik SE. A distributed optical fiber sensor for temperature detection in power cables. Sensors and Actuators, A: Physical. 2006;**125**:148-155. DOI: 10.1016/j.sna.2005.06.024

[9] Wang ZL, Zhang SS, Chang J. Attenuation auto-correction method in Raman distributed temperature measurement system. Optical and Quantum Electronics. 2013;**45**:1087-1094. DOI: 10.1007/s11082-013-9720-2

[10] Hill K, Fujii Y, Johnson DC. Photosensitivity in optical fiber waveguides: Application to reflection filter fabrication. Applied Physics Letters. 1978;**32**:647-649. DOI: 10.1063/1.89881

[11] Culshaw B. Fiber optics in sensing and measurement. IEEE Journal of Selected Topics in Quantum Electronics. 2000;**6**:1014-1021. DOI: 10.1109/2944.902150

[12] Bolshov M, Kuritsyn YA, Romanovskii YV. Tunable diode laser spectroscopy as a technique for combustion diagnostics. Spectrochimica Acta Part B: Atomic Spectroscopy. 2015;**106**:45-66. DOI: 10.1016/j.sab.2015.01.010

[13] Ouyang X, Varghese PL. Line-of-sight absorption measurements of high temperature gases with thermal and concentration boundary layers. Applied Optics. 1989;**28**:3979-3984. DOI: 10.1364/AO.28.003979

[14] Zhou X, Liu X, Jeffries JB. Development of a sensor for temperature and water concentration in combustion gases using a single tunable diode laser. Measurement Science and Technology. 2003;**14**:1459-1468. DOI: 10.1088/0957-0233/14/8/335

[15] Liu X, Jeffries JB, Hanson RK. Measurement of non-uniform temperature distributions using line-of-sight absorption spectroscopy. AIAA Journal. 2007;**45**:411-419. DOI: 10.2514/1.26708

[16] Zhang G, Liu J, Xu Z. Characterization of temperature non-uniformity over a premixed CH4–air flame based on line-of-sight TDLAS. Applied Physics B. 2016;**122**:9. DOI: 10.1007/s00340-015-6289-4

[17] Busa KM, Bryner E, McDaniel JC. Demonstration of capability of water flux measurement in a scramjet combustor using tunable diode laser absorption tomography and stereoscopic PIV. 49th AIAA Aerospace Sciences Meeting Including the New Horizons Forum and Aerospace Exposition; 2011. pp. 1-14

[18] Busa KM, Ellison EN, McGovern BJ. Measurements on NASA Langley durable combustor rig by TDLAT: Preliminary results. 51st AIAA Aerospace Sciences Meeting Including New Horizons Forum and Aerospace Exposition, AIAA-2013-06962013

[19] Ma L, Li X, Sanders ST. 50-kHz-rate 2D imaging of temperature and H_2O concentration at the exhaust plane of a J85 engine using hyperspectral tomography. Optics Express. 2013; **21**:1152-1162. DOI: 10.1364/OE.21.001152

[20] Busa KM, Rice BE, McDaniel JC. Direct measurement of combustion efficiency of a dual-mode Scramjet via TDLAT and SPIV. 53rd AIAA Aerospace Sciences Meeting; 2015. p. 0357

[21] Sun P, Zhang Z, Li Z. A study of two dimensional tomography reconstruction of temperature and gas concentration in a combustion field using TDLAS. Applied Sciences. 2017;**7**. DOI: 10.3390/app7100990

[22] Suh K, Lee C. Auto-correction method for differential attenuation in a fiber-optic distributed-temperature sensor. Optics Letters. 2008;**33**:1845-1847. DOI: 10.1364/OL.33.001845

[23] Fernandez A, Rodeghiero P, Brichard B, et al. Radiation tolerant Raman distributed temperature monitoring system for large nuclear infrastructures. IEEE Transactions on Nuclear Science. 2005;**52**:2689-2694. DOI: 10.1109/TNS.2005.860736

[24] Sun BN, Chang J, Lian J. Accuracy improvement of Raman distributed temperature sensors based on eliminating Rayleigh noise impact. Optics Communication. 2013;**306**: 117-120. DOI: 10.1016/j.optcom.2013.05.049

[25] Kwon H, Kim S, Yeom S. Analysis of nonlinear fitting methods for distributed measurement of temperature and strain over 36km optical fiber based on spontaneous Brillouin backscattering. Optics Communication. 2013;**294**:59-63. DOI: 10.1016/j.optcom.2012.12.012

[26] Wang ZL, Chang J, Zhang SS. Spatial resolution improvement of distributed Raman temperature measurement system. IEEE Sensors Journal. 2013;**13**:4271-4278. DOI: 10.1109/jsen.2013.2263380

[27] Sun M, Tang Y, Yang S. Fire source localization based on distributed temperature sensing by a dual-line optical fiber system. Sensors (Basel). 2016;**16**:829. DOI: 10.3390/s16060829

[28] Sun M, Tang Y, Yang S. Fiber optic distributed temperature sensing for fire source localization. Measurement Science and Technology. 2017;**28**:085102. DOI: 10.1088/1361-6501/aa7436

[29] Wang S, Berentsen M, Kaiser T. Signal processing algorithms for fire localization using temperature sensor arrays. Fire Safety Journal. 2005;**40**:689-697. DOI: 10.1016/j.firesaf.2005.06.004

[30] Kersey AD, Davis MA, Patrick HJ. Fiber grating sensors. Journal of Lightwave Technology. 1997;**15**:1442-1463. DOI: 10.1109/50.618377

[31] Yariv A. Coupled-mode theory for guided-wave optics. IEEE Journal of Quantum Electronics. 1973;**9**:919-933. DOI: 10.1109/Jqe.1973.1077767

[32] Kashyap R. Chapter 4 - Theory of Fiber Bragg Gratings. Fiber Bragg Gratings. San Diego: Academic Press; 1999. p. 119-193. DOI: 10.1016/B978-012400560-0/50005-1

[33] Othonos A, Kalli K. Fiber Bragg Gratings: Fundamentals and Applications in Telecommunications and Sensing. Boston: Artech House; 1999. DOI: 10.1063/1.883086

[34] Xu M, Reekie L, Chow Y. Optical in-fibre grating high pressure sensor. Electronics Letters. 1993;**29**:398-399. DOI: 10.1049/el:19930267

[35] Malitson I. Interspecimen comparison of the refractive index of fused silica. JOSA. 1965;**55**: 1205-1209. DOI: 10.1364/JOSA.55.001205

[36] Wemple S. Refractive-index behavior of amorphous semiconductors and glasses. Physical Review B. 1973;**7**:3767. DOI: 10.1103/PhysRevB.7.3767

[37] Takahashi S, Shibata S. Thermal variation of attenuation for optical fibers. Journal of Non-Crystalline Solids. 1979;**30**:359-370. DOI: 10.1016/0022-3093(79)90173-X

[38] Jung J, Nam H, Lee B. Fiber Bragg grating temperature sensor with controllable sensitivity. Applied Optics. 1999;**38**:2752-2754. DOI: 10.1364/AO.38.002752

[39] Yang S, Li J, Tang Y. Analysis of the performance of strain magnification using uniform rectangular cantilever beam with fiber Bragg gratings. Sensors and Actuators A: Physical. 2018;**273**:266-275. DOI: 10.1016/j.sna.2018.01.017

[40] Meltz G, Morey WW, Glenn W. Formation of Bragg gratings in optical fibers by a transverse holographic method. Optics Letters. 1989;**14**:823-825. DOI: 10.1364/OL.14.000823

[41] Hill K, Malo B, Vineberg K. Efficient mode conversion in telecommunication fibre using externally written gratings. Electronics Letters. 1990;**26**:1270-1272. DOI: 10.1049/el:19900818

[42] Hill KO, Malo B, Bilodeau F. Bragg gratings fabricated in monomode photosensitive optical fiber by UV exposure through a phase mask. Applied Physics Letters. 1993;**62**: 1035-1037. DOI: 10.1063/1.108786

[43] Maaskant R, Alavie T, Measures R. Fiber-optic Bragg grating sensors for bridge monitoring. Cement and Concrete Composites. 1997;**19**:21-33. DOI: 10.1016/S0958-9465(96)00040-6

[44] Tennyson R, Mufti A, Rizkalla S. Structural health monitoring of innovative bridges in Canada with fiber optic sensors. Smart Materials and Structures. 2001;**10**:560. DOI: 10.1088/0964-1726/10/3/320

[45] Hirayama N, Sano Y. Fiber Bragg grating temperature sensor for practical use. ISA Transactions. 2000;**39**:169-173. DOI: 10.1016/S0019-0578(00)00012-4

[46] Fokine M. Thermal stability of chemical composition gratings in fluorine–germanium-doped silica fibers. Optics Letters. 2002;**27**:1016-1018. DOI: 10.1364/OL.27.001016

[47] Dragomir A, Nikogosyan DN, Zagorulko KA. Inscription of fiber Bragg gratings by ultraviolet femtosecond radiation. Optics Letters. 2003;**28**:2171-2173. DOI: 10.1364/OL.28.002171

[48] Lowder TL, Smith KH, Ipson BL. High-temperature sensing using surface relief fiber Bragg gratings. IEEE Photonics Technology Letters. 2005;**17**:1926-1928. DOI: 10.1109/Lpt.2005.852646

[49] Sampath U, Kim D, Kim H. Polymer-coated FBG sensor for simultaneous temperature and strain monitoring in composite materials under cryogenic conditions. Applied Optics. 2018;**57**. DOI: 10.1364/ao.57.000492

[50] Yun-Jiang R, Webb DJ, Jackson DA. In-fiber Bragg-grating temperature sensor system for medical applications. Journal of Lightwave Technology. 1997;**15**:779-785. DOI: 10.1109/50.580812

[51] Moyo P, Brownjohn JMW, Suresh R. Development of fiber Bragg grating sensors for monitoring civil infrastructure. Engineering Structures. 2005;**27**:1828-1834. DOI: 10.1016/j.engstruct.2005.04.023

[52] Fernandez AF, Brichard B, Borgermans P. 15th: IEEE fibre Bragg grating temperature sensors for harsh nuclear environments. Optical Fiber Sensors Conference Technical Digest, 2002 Ofs 2002; 2002. pp. 63-66

[53] Lee J-H, Kim S-G, Park H-J. Investigation of Fiber Bragg grating temperature sensor for applications in electric power systems. 2006 8th International Conference on Properties and Applications of Dielectric Materials. IEEE; 2006. pp. 431-434

[54] Yang S, Li J, Xu S. Temperature insensitive measurements of displacement using fiber Bragg grating sensors. Advanced Sensor Systems and Applications VII: International Society for Optics and Photonics. 2016. p. 1002504

[55] Zhang Y, Yang W. Simultaneous precision measurement of high temperature and large strain based on twisted FBG considering nonlinearity and uncertainty. Sensors and Actuators, A: Physical. 2016;**239**:185-195. DOI: 10.1016/j.sna.2016.01.012

[56] Li T, Tan Y, Han X. Diaphragm based fiber Bragg grating acceleration sensor with temperature compensation. Sensors (Basel). 2017;**17**. DOI: 10.3390/s17010218

[57] Li C, Ning T, Zhang C. Liquid level measurement based on a no-core fiber with temperature compensation using a fiber Bragg grating. Sensors and Actuators, A: Physical. 2016;**245**:49-53. DOI: 10.1016/j.sna.2016.04.046

[58] Witzel O, Klein A, Meffert C. VCSEL-based, high-speed, in situ TDLAS for in-cylinder water vapor measurements in IC engines. Optics Express. 2013;**21**:19951-19965. DOI: 10.1364/Oe.21.019951

[59] Bolshov MA, Kuritsyn YA, Liger VV. Measurements of the temperature and water vapor concentration in a hot zone by tunable diode laser absorption spectrometry. Applied Physics B: Lasers and Optics. 2010;**100**:397. DOI: 10.1007/s00340-009-3882-4

[60] Sane A, Satija A, Lucht RP. Simultaneous CO concentration and temperature measurements using tunable diode laser absorption spectroscopy near 2.3 μm. Applied Physics B. 2014;**117**:7-18. DOI: 10.1007/s00340-014-5792-3

[61] Webber ME. Diode laser measurements of NH_3 and CO_2 for combustion and bioreactor applications [Thesis]. Stanford University; 2001

[62] Gamache RR, Kennedy S, Hawkins R. Total internal partition sums for molecules in the terrestrial atmosphere. Journal of Molecular Structure. 2000;**517**:407-425. DOI: 10.1016/s0022-2860(99)00266-5

[63] Liu X, Jeffries JB, Hanson RK. Development of a tunable diode laser sensor for measurements of gas turbine exhaust temperature. Applied Physics B. 2005;**82**:469-478. DOI: 10.1007/s00340-005-2078-9

[64] Wang F, Cen KF, Li N. Two-dimensional tomography for gas concentration and temperature distributions based on tunable diode laser absorption spectroscopy. Measurement Science and Technology. 2010;**21**:045301. DOI: 10.1088/0957-0233/21/4/045301

[65] Herman GT, Lent A, Lutz PH. Relaxation methods for image reconstruction. Communications of the ACM. 1978;**21**:152-158. DOI: 10.1145/359340.359351

[66] Li N, Weng C. Modified adaptive algebraic tomographic reconstruction of gas distribution from incomplete projection by a two-wavelength absorption scheme. Chinese Optics Letters. 2011;**9**:061201. DOI: 10.3788/COL201109.061201

[67] Kasyutich VL, Martin PA. Towards a two-dimensional concentration and temperature laser absorption tomography sensor system. Applied Physics B. 2011;**102**:149-162. DOI: 10.1007/s00340-010-4123-6

IntechOpen